SUPPLEMENTARY MATERIAL

Hubbard band *vs.* oxygen vacancy states in the correlated electron metal SrVO$_3$

S. Backes,[1, *] T. C. Rödel,[2, 3, *] F. Fortuna,[2] E. Frantzeskakis,[2] P. Le Fèvre,[3] F. Bertran,[3]

M. Kobayashi,[4] R. Yukawa,[4] T. Mitsuhashi,[4] M. Kitamura,[4] K. Horiba,[4] H. Kumigashira,[4]

R. Saint-Martin,[5] A. Fouchet,[6] B. Berini,[6] Y. Dumont,[6] A. J. Kim,[1] F. Lechermann,[7, 8]

H. O. Jeschke,[1] M. J. Rozenberg,[9] R. Valentí,[1, †] and A. F. Santander-Syro[2, ‡]

[1]*Institut für Theoretische Physik, Goethe-Universität Frankfurt,*
Max-von-Laue-Str. 1, 60438 Frankfurt am Main, Germany

[2]*CSNSM, Univ. Paris-Sud, CNRS/IN2P3,*
Université Paris-Saclay, 91405 Orsay Cedex, France

[3]*Synchrotron SOLEIL, L'Orme des Merisiers,*
Saint-Aubin-BP48, 91192 Gif-sur-Yvette, France

[4]*Photon Factory, Institute of Materials Structure Science,*
High Energy Accelerator Research Organization (KEK),
1-1 Oho, Tsukuba 305-0801, Japan

[5]*SP2M-ICMMO - UMR-CNRS 8182 Université Paris-Sud,*
Université Paris-Saclay, 91405 Orsay Cedex, France

[6]*GEMaC, Université de Versailles St. Quentin en Y. - CNRS,*
Université Paris-Saclay, Versailles, France

[7]*Institut für Theoretische Physik, Universität Hamburg,*
Jungiusstrasse 9, 20355 Hamburg, Germany

[8]*Institut für Keramische Hochleistungswerkstoffe,*
TU Hamburg-Harburg, D-21073 Hamburg, Germany

[9]*Laboratoire de Physique des Solides, CNRS, Univ. Paris-Sud,*
Université Paris-Saclay, 91405 Orsay Cedex, France.

EXPERIMENTAL METHODS

Sample preparation

The SrVO$_3$ thin films measured at SOLEIL (CASSIOPEE Beamline) were grown at the GEMaC laboratory, onto atomically flat TiO$_2$-terminated (100) SrTiO$_3$ substrates by pulsed laser deposition (PLD) under a partial oxygen pressure of 5×10^{-6} Torr at 750°C. A 248 nm wavelength KrF excimer laser was employed with a repetition rate of 1 Hz and a fluency of 1.9 J/cm^2. During the growth, surface structure was characterized by Reflection High-Energy Electron Diffraction (RHEED). After the growth, oxygen pressure was reduced to 5×10^{-8} Torr when the sample was cooled to room temperature. Surface morphology was carried out with atomic force microscopy (AFM, Bruker Dimension 3100) in tapping mode and the Root Mean Square (rms) roughness of the film was 0.4 nm. To clean the surfaces in UHV prior to ARPES experiments at SOLEIL, the SrVO$_3$ thin films were annealed at a temperature $T = 550$ °C for $t = 5 - 20$ min at pressures lower than $p < 2 \times 10^{-8}$ Torr. One of the samples was Ar$^+$ sputtered ($U = 1000$ V, $t = 7$ min) prior to the UHV annealing, without noticeable changes in the ARPES data. After the UHV annealing, the quality of the surfaces was confirmed by low-energy electron diffraction (LEED).

The SrVO$_3$ films measured at KEK (beamline 2A) were grown *in situ*, in a PLD chamber directly accessible from the ARPES UHV chamber, on single-crystalline 0.05 wt% Nb-doped SrTiO$_3$ (001) substrates. The substrates were annealed at 1050°C under an oxygen pressure of $\sim 8 \times 10^{-8}$ Torr to obtain atomically flat TiO$_2$-terminated surfaces. The SrVO$_3$ thin film was deposited on the substrate at 850°C, under a high vacuum below $\sim 10^{-7}$ Torr, to obtain an UHV clean surface, using a Sr$_2$V$_2$O$_7$ target, which has excess oxygen with respect to SrVO$_3$, and thus minimizes the formation of vacancies during the growth. LEED measurements confirmed clean cristalline SrVO$_3$ films with a $c(4 \times 4)$ surface reconstruction. The surface morphology of the measured thin films was confirmed by *ex situ* atomic force microscopy, showing atomically flat step-and-terrace structures. The coherent growth of these SrVO$_3$ thin films was confirmed by four-circle X-ray diffraction measurements. The characterization results are essentially identical to those reported in previous studies [SR1, SR2, SR3], and indicate that there are no detectable structural disorders in the prepared SrVO$_3$ thin films grown on Nb:SrTiO$_3$ (001) substrates.

ARPES measurements

The ARPES measurements were conducted at the CASSIOPEE beamline of Synchrotron SOLEIL (France), and at the beamline 2A of KEK-Photon Factory (KEK-PF, Japan). We used linearly polarized photons in the energy range $30 - 110$ eV and hemispherical electron analyzers with vertical slits at SOLEIL and horizontal slits at KEK-PF. The angular and energy resolutions were $0.25°$ and 15 meV. The mean diameter of the incident photon beam was smaller than 100 μm. The UV light brilliance, measured using calibrated photodiodes, was $\approx 5 \times 10^9$ photons $s^{-1}\mu m^{-2}$ at SOLEIL, and about 100 times smaller at KEK-PF. The (001) oriented $SrVO_3$ samples were cooled down to $T = 20$ K before measuring. Unless specified otherwise, all data was taken at that temperature. Measuring at such low temperature minimizes any possible diffusion of oxygen vacancies into the bulk. The results have been reproduced on more than 5 samples. All through this paper, directions and planes are defined in the cubic unit cell of $SrVO_3$. We note $[hkl]$ the crystallographic directions in real space, $\langle hkl \rangle$ the corresponding directions in reciprocal space, and (hkl) the planes orthogonal to those directions. The indices h, k, and l of Γ_{hkl} correspond to the reciprocal lattice vectors of the cubic unit cell of $SrVO_3$.

SURFACE UMKLAPP BANDS IN THIN FILMS OF SrVO$_3$

The surface reconstruction in $SrVO_3$ thin films leads to the occurence of surface umklapp bands in the ARPES spectra, as shown in Figs. S1(a, b) for data taken with linear horizontal and linear vertical photons polarizations, respectively. These extra bands, best observed with linear horizontal photons, result simply from the folding of the bulk bands at the surface due to the superposition of the bulk and the reconstructed surface periodicities. Their presence is a final-state effect and does not affect the bulk electronic structure or the effects due to oxygen vacancies discussed in this work. Note that the spectra taken with linear vertical photons show both the light and heavy bands expected for the intrinsic bulk electronic structure of $SrVO_3$, discussed in the next section.
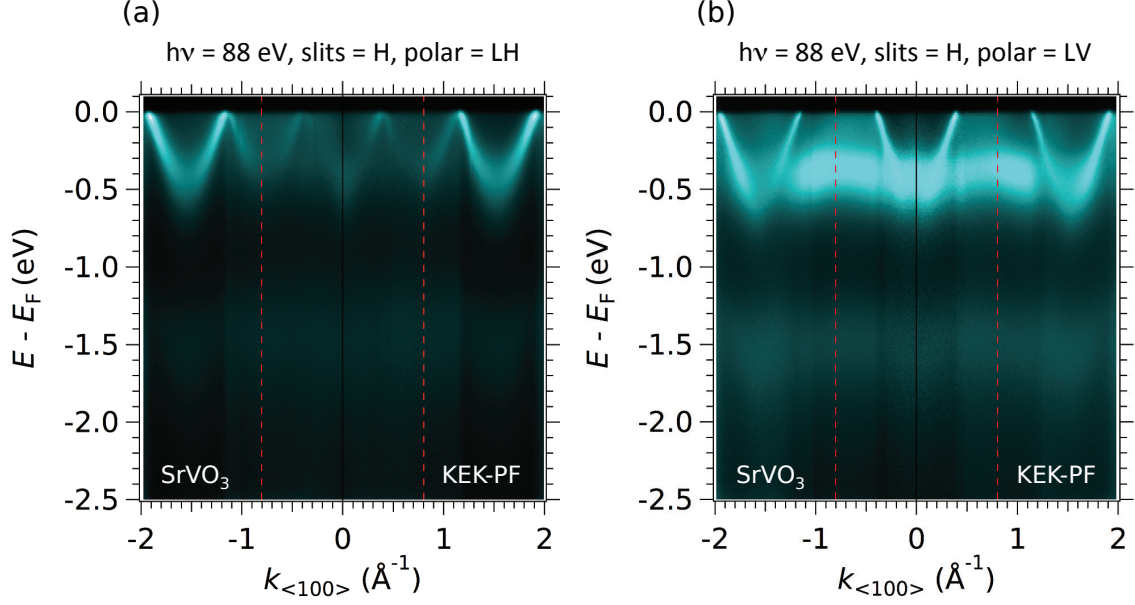
3

Figure S 1. Energy-momentum ARPES intensity maps spanning 3 consecutive Brillouin zones on an SrVO$_3$ thin film prepared *in situ*. Vertical dashed red lines show the edges of the bulk unreconstructed Brillouin-zone. The data were measured at KEK-PF using $h\nu = 88$ eV photons with (a) linear horizontal and (b) linear vertical polarizations, and a hemispherical electron analyzer with horizontal slits. The sample temperature was 20 K. Surface umklapp bands induced by the surface reconstruction are best observed in the data using linear horizontal polarization. The spectra taken with linear vertical photons reveal the light and heavy bands of the intrinsic bulk electronic structure of SrVO$_3$.

BULK ELECTRONIC STRUCTURE OF SrVO$_3$

Bulk light and heavy bands

Figure S2 presents a zoom around Γ of the ARPES energy-momentum map shown in Fig. S1(b), which was taken using linear vertical photons and a hemispherical electron analyzer with horizontal slits. This configuration of experimental geometry and light polarization allows observing both the light and heavy conduction bands of SrVO$_3$. We fit these bands using simple cosine dispersions of the form $E(k) = E_0 - 2t\cos(ka)$, where E_0 is a constant, $4t$ is the bandwidth, and a is the in-plane lattice parameter of the SrVO$_3$ thin films ($a = 3.905$ Å in the case of films grown on SrTiO$_3$). For small ka, each cosine band can be approximated by a free-electron-like parabola of effective mass $m^\star$ given by
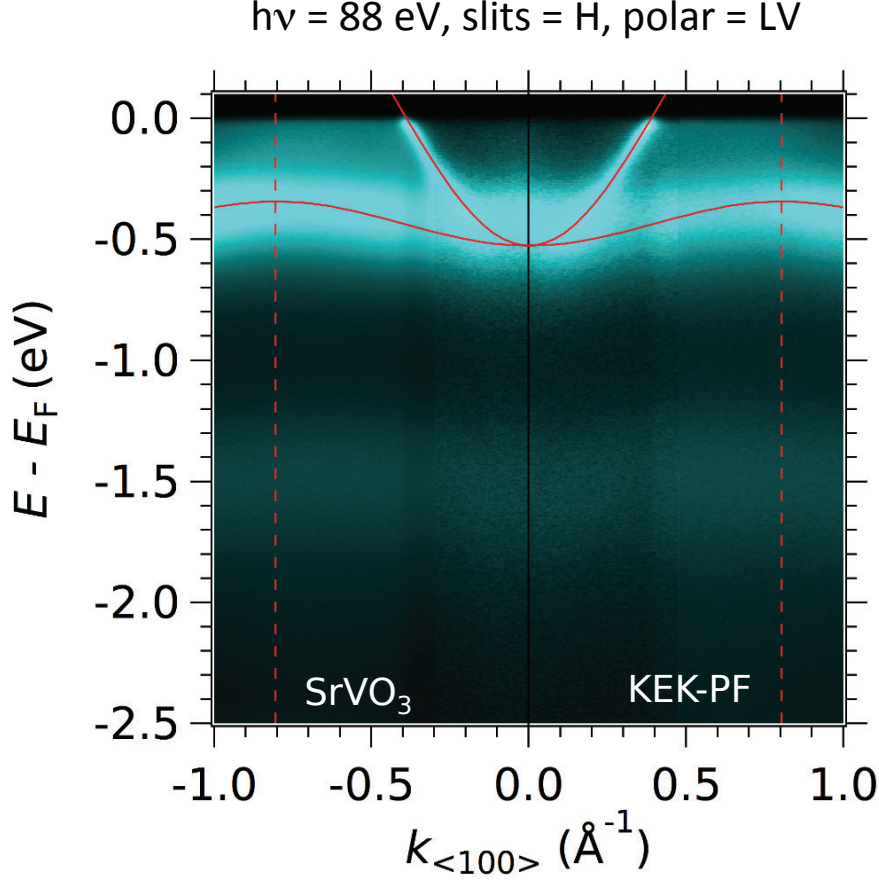
hν = 88 eV, slits = H, polar = LV

Figure S 2. Zoom around Γ of the energy-momentum ARPES intensity map shown in Fig. S1(b), measured at KEK-PF using $h\nu = 88$ eV photons with linear vertical polarization and a hemispherical electron analyzer with horizontal slits. Vertical dashed red lines show the Brillouin-zone edges. Continuous red curves are cosine fits to the bands.

$ta^2 = \hbar^2/(2m^\star)$. The best fits, shown by the continuous red curves in Fig. S2, yield effective masses $m_l^\star = 0.9m_e$ and $m_h^\star = 5.5m_e$ for the light and heavy bands, respectively (m_e is the free electron mass).

3D k-space mapping

For electrons at E_F, within the free-electron final state model, ARPES measurements at constant photon energy give the electronic structure at the surface of a spherical cap of radius $k = \sqrt{\frac{2m_e}{\hbar^2}}\left(h\nu - \Phi + V_0\right)^{1/2}$. Here, m_e is the free electron mass, Φ is the work
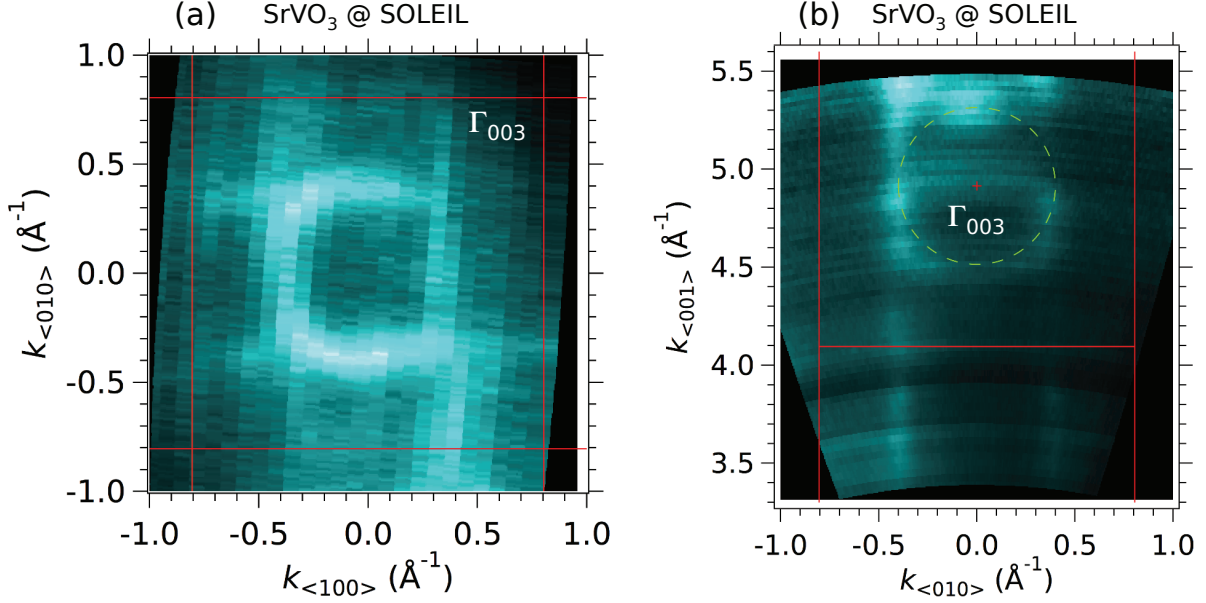
Figure S 3. (a) In-plane Fermi-surface of $SrVO_3(001)$, measured using linear horizontal photons at $h\nu = 72$ eV, and a hemispherical electron analyzer with vertical slits. (b) Out-of-plane Fermi surface of $SrVO_3(001)$, measured using linear vertical photons from 30 eV to 95 eV, in steps of 1 eV, and a hemispherical electron analyzer with vertical slits. The green dashed circle is as guide to the eye showing the quasi-circular Fermi-surface formed by the d_{yz} states. In both panels, the red lines delimit the Brillouin-zone. All data from this figure were measured at CASSIOPEE (SOLEIL), using the same conditions of light brilliance of Figs. 2(a, b) of the main text.

function, and $V_0 = 18$ eV is the "inner potential" of $SrVO_3$ [SR5]. Measurements around normal emission provide the electronic structure in a spherical cap nearly parallel to the surface plane ($k_x - k_y$ plane), such as the one around Γ_{003} shown in Fig. S3(a) Likewise, measurements as a function of photon energy provide the electronic structure in the plane defined by the surface normal and the analyzer's slit direction ($k_y - k_z$ plane), presented in Fig. S3(b).

As was shown in Figs. 2(a, b) of the main text, the Fermi momenta and band filling of the quasiparticle (QP) conduction band are independent of the UV dose. This ensures that the Fermi surface maps are exempt of extrinsic spurious effects due to the UV-assisted creation of oxygen vacancies.

Our measured Fermi surface, Figs. S3(a, b) agrees with previous ARPES reports on the

electronic structure of SrVO$_3$ [SR4, SR5, SR6]. Furthermore, the bulk 3D character of our measured Fermi surface is demonstrated by the observation, in Fig. S3(b), of dispersive d_{yz} states forming a quasi-circular Fermi sheet in the $k_y - k_z$ plane (green dashed circle serving as guide to the eye).

The 3D density of carriers in the bulk conduction band (n_{3D}) can be directly calculated from the volume enclosed by the measured Fermi surface (V_F) as $n_{3D} = V_F/4\pi^3$. In very good approximation, V_F corresponds to the volume of three mutually orthogonal inter-penetrating cylinders of cross-sectional Fermi radius $k_F = 0.4$ Å^{-1} and length $2\pi/a$ (a is the cubic lattice constant of SrVO$_3$), *i.e.*: $V_F \approx 3 \times \pi k_F^2 \times 2\pi/a - 2 \times (4/3)\pi k_F^3$, where the last term avoids counting three times the inner Fermi quasi-sphere at the intersection of the three cylinders. This gives $n_{3D} \approx 0.9e^-/a^3$ (a^3 is the unit-cell volume), which is in excellent agreement with the expected value of 1 electron per Vanadium. This again confirms that our ARPES measurements probe the 3D bulk Fermi surface.

ELECTRONIC STRUCTURE OF "VACANCY-FREE" SrVO$_3$ USING LOW-DOSE UV LIGHT

Fig. S4 shows momentum-integrated photoemission spectra of a bulk SrVO$_3$/SrTiO$_3$ thin-film prepared and measured *in situ* at KEK-PF. This eliminates the need to re-anneal in vacuum to clean the surface, and thus minimizes the formation of oxygen vacancies before the measurements. Additionally, the spectra were measured using doses of UV light which were about 100 times smaller than the ones used in figure 2 of the main text. As can be seen from the figure, this careful measurement protocol prevents the formation of oxygen vacancies, allowing to acquire high-quality data that shows no significant evolution with accumulation time, even after several hours of measurements. Thus, we define the obtained spectra as the "intrinsic" (occupied part of the) spectral function of SrVO$_3$, modulo matrix elements inherent to the photoemission process itself.

RAW ARPES EDCS: "VACANCY-FREE" *VS* VACANCY-FULL SrVO$_3$

Fig. S5(a) shows the raw ARPES energy distribution curves (EDCs) for the QP and lower Hubbard band dispersions in a sample with a negligible concentration of vacancies measured
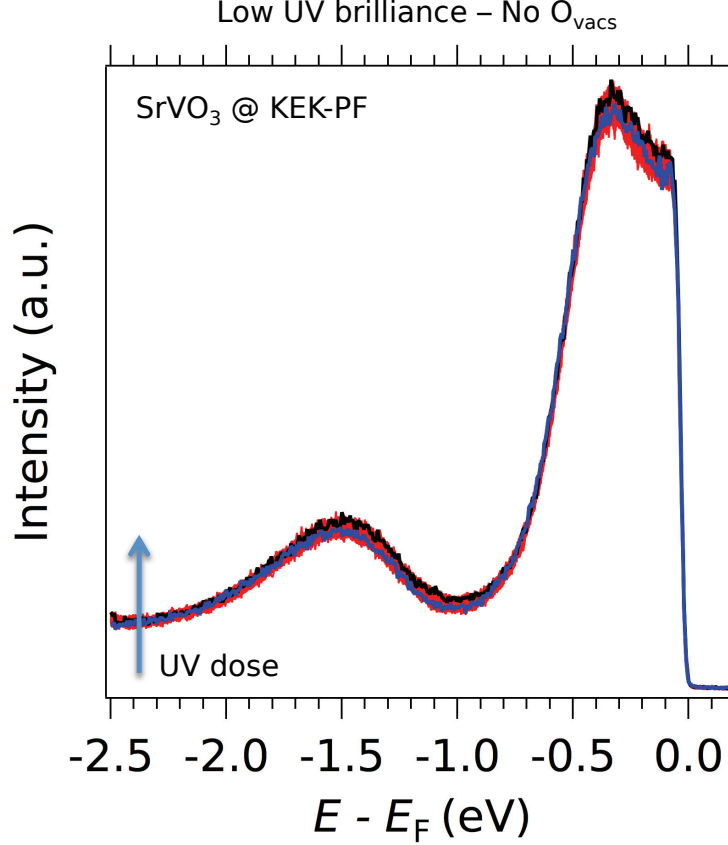
Figure S 4. Photoemission spectra of $SrVO_3$ as a function of irradiation time using a low dose of UV light. The sample was prepared *in situ*. This eliminates the need to re-anneal in vacuum to clean the surface prior to measurements, and thus minimizes the formation of oxygen vacancies. The energy distribution curves (EDCs) were extracted from ARPES data around the Γ_{003} point integrated along the $k = <100>$ direction. The blue and black curves show spectra for the lowest and highest measured doses, obtained respectively after ~ 2 minutes and ~ 2 hours of irradiation. The data from this figure were measured at beamline 2A of KEK-PF using $h\nu = 88$ eV photons with linear horizontal polarization, and a hemispherical electron analyzer with horizontal slits.

under low UV dose, corresponding to the data of Figs. 3(a, b) of the main text. Fig. S5(b) shows the energy-momentum ARPES intensity map of the previous plot, using a second-derivative representation. The use of second derivatives in the ARPES data allows a good visualization of the dispersion of both the quasi-particle and the Mott-Hubbard bands on the same color plot, despite their very dissimilar raw intensities. The dispersionless feature at E_F is a spurious effect of such second-derivative on the Fermi-Dirac cutoff. Likewise,
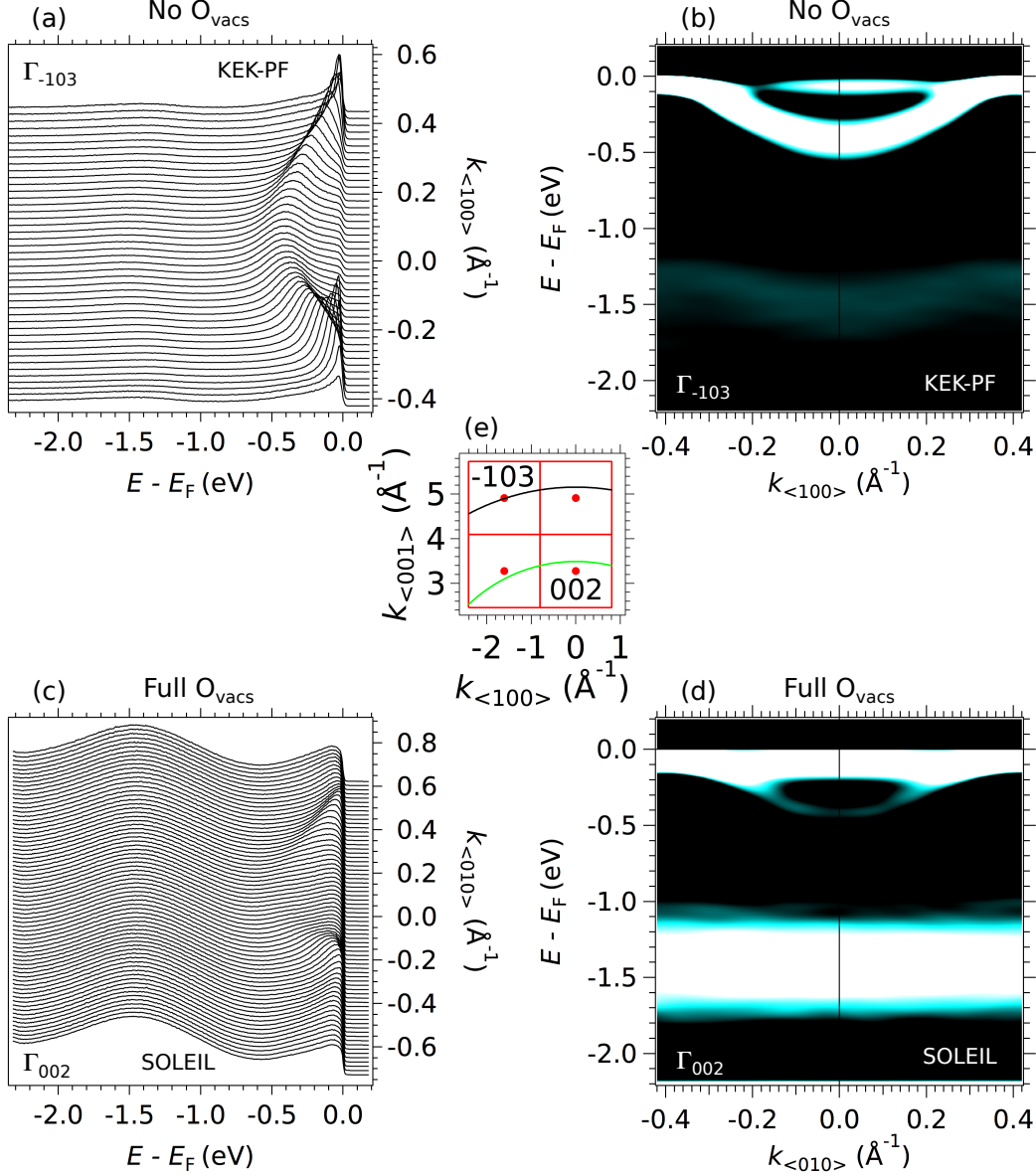
Figure S 5. (a) Raw EDCs of the energy-momentum ARPES intensity map measured at a low UV dose on a $SrVO_3$ sample prepared *in situ*. The data were obtained at the beamline 2A of KEK-PF using $h\nu = 88$ eV photons with linear horizontal polarization, and a hemispherical electron analyzer with horizontal slits. (b) Second derivative (negative values) of the energy-momentum ARPES intensity map from (a). (c, d) Same as (a, b) after a strong UV irradiation. This data were measured at CASSIOPEE (SOLEIL) using $h\nu = 33$ eV photons with linear vertical polarization, and a hemispherical electron analyzer with vertical slits. (e) ARPES measurement arcs for $h\nu = 33$ eV (green) and $h\nu = 88$ eV (black), which come close to the Γ_{002} and $\Gamma_{\bar{1}03}$ points, respectively. Red rectangles show the Brillouin zone edges. All data were taken at 20 K.

Figs. S5(c, d) show the raw ARPES EDCs, and associated second-derivative plot, for the QP and in-gap state for a sample exposed to a strong UV dose, all corresponding to the data of Figs. 3(c, d) of the main text. The larger amount of vacancies enhances the background of inelastic electron scattering, as seen from panel (c), hence increasing the height of the Fermi-Dirac step and the intensity of the spurious feature at E_F in the second-derivative plot, panel (d). Fig. S5(e) specifies the points and directions of measurements in 3D k-space for the data from SOLEIL (green arc) and KEK-PF (black arc).

As mentioned in the main text, in the sample with a negligible concentration of vacancies the QP band and lower Hubbard band show the same dispersion, while in the sample that has been strongly irradiated, and has thus a large concentration of oxygen vacancies, the peak at -1.5 eV becomes broader, more intense, and non-dispersive.

THEORETICAL METHODS

LDA and LDA+DMFT Calculations

For the DFT in the local density approximation (LDA) and LDA+DMFT calculations we consider a $2 \times 2 \times 3$ supercell where two adjacent oxygen atoms to a vanadium have been removed. This leads to a stripe-like configuration of vacancies with a concentration of $2/36 \approx 5.56\%$. The internal atomic positions of this structure has been relaxed using the GPAW code [SR7].

For the LDA+DMFT calculations (see Ref. [SR8] for a detailed explanation) we used the WIEN2K [SR9] implementation in the local density approximation in combination with a continuous-time quantum Monte Carlo (CTQMC) impurity solver in the hybridization expansion [SR10] from the ALPS [SR11, SR12] project. We projected the Bloch wave functions onto localized V $3d$ orbitals [SR13, SR14] in the unit cell, leading to a set of 6 inequivalent impurities for the two vacancy structure. Within the DMFT approximation we assume that (i) the multiple impurity atoms only hybridize with an effective bath that is determined self-consistently and (ii) the intersite hybridization to be small. This allows us to solve the impurity problems separately and to write the full self-energy in Bloch space as

$$\Sigma_{\nu\nu'}(k, i\omega_n) = \left(\sum_a P_a^\dagger(k) \Sigma_a(i\omega_n) P_a(k) \right)_{\nu\nu'}, \tag{1}$$

where the sum is performed over all impurity atoms a, with the corresponding projection operators $P_a(k)$. The projection comprises the V t_{2g} and e_g orbitals in the energy window $[-1.5, 6.0]$ eV. The calculations were performed for the inverse temperature $\beta = 40\,\text{eV}^{-1}$ (290 K) with the interaction parameters used in the definition of the Slater integrals [SR15] with average $U = 2.5\,\text{eV}$ and $J_H = 0.6\,\text{eV}$. For the double counting correction we used the FLL [SR16, SR17] scheme and we checked that different values of the double counting only lead to small quantitative changes in the spectral function. We perfomed analytic continuation directly on the impurity self-energies $\Sigma_a(i\omega_n)$ by stochastic analytic continuation [SR18] to obtain $\Sigma_a(\omega)$ on the real axis. By this, the spectral function in Bloch space is given by

$$A(k, \omega) = -\frac{1}{\pi}\text{Im } G(\omega) \tag{2}$$

$$= -\frac{1}{\pi}\text{Im } \left(\left[(\omega + \mu)\mathbb{1} - H_{LDA}(k) - \sum_a P_a^\dagger(k)\Sigma_a(\omega)P_a(k) \right]^{-1} \right), \tag{3}$$

where $G(\omega)$ is the interacting Green's function, or respectively, the atom- and orbital resolved spectral function

$$A(k, \omega) = -\frac{1}{\pi}\text{Im } \left(P_a(k)G(\omega)P_a^\dagger(k) \right). \tag{4}$$

In the main text and the supplementary material we always show the atom- and orbital resolved spectral function of the t_{2g} and e_g states summed over all atoms.

Standard LDA+DMFT vs. LDA+DMFT including dynamical screening

In this work we included the effects of bandwidth renormalization due to dynamically screened Coulomb interactions using a low-energy effective model with an effective Hamiltonian

$$H_{eff} = -\sum_{ij\sigma} Z_B t_{ij} d_{i\sigma}^\dagger d_{i\sigma} + U_0 \sum_i d_{i\uparrow}^\dagger d_{i\uparrow} d_{i\downarrow}^\dagger d_{i\downarrow}, \tag{5}$$

with the screened Hubbard interaction U_0. This approach has been suggested in Ref. [SR19], and proved to be a good approximation to the full treatment of the dynamically screened Coulomb interaction. For the bandwidth renormalization factor we used $Z_B = 0.7$ [SR19].

In Fig. S6 we show a comparison between standard DFT, "standard" LDA+DMFT and the LDA+DMFT approach including the effective screening of the Coulomb interaction for
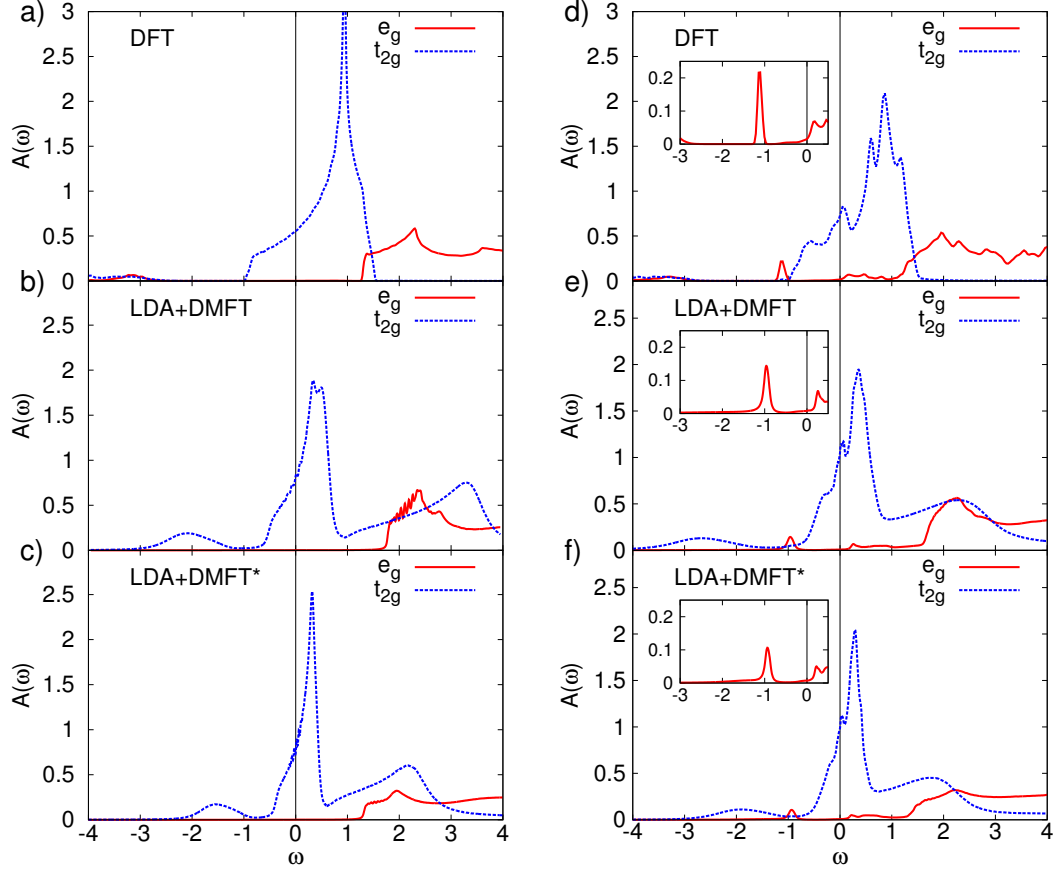
Figure S 6. (Color online) Comparison for bulk $SrVO_3$ between (a) the DFT result, (b) the LDA+DMFT result, and (c) the LDA+DMFT including an effective treatment of the dynamical Coulomb interacting screeening (explained in the main text) indicated by a *. (d-f): Same comparison for the 2 vacancy structure of $SrVO_3$. The main effect of the renormalization factor is a shift of the upper and lower t_{2g} Hubbard bands towards the Fermi level, yielding a better agreement with experiment.

a)-c) bulk $SrVO_3$ and d)-f) the two vacancy structure of $SrVO_3$. The main effect of including the Coulomb interaction screening via this approach is a shift of the upper and lower t_{2g} Hubbard bands towards the Fermi level, originating from the effective reduction of bandwidth. Compared to experiment (as discussed in the main text), "standard" LDA+DMFT consistently locates the lower Hubbard band at higher binding energies, in both the bulk and vacancy structure, whereas the effective model yields a much better agreement. Especially in the bulk system the position of the lower Hubbard band is brought to a good agreement.

Finally, the calculations with oxygen vacancies produce a ladder of heavy bands near E_F, that originate from the non-equivalency in all the vanadium atoms of the super-cell contributing t_{2g} bands near the Fermi level. This V non-equivalency is due to the presence of oxygen vacancies that lower the symmetry. In the more realistic case with larger cells, only the in-gap e_g states of the V near the vacancy/vacancies would produce a significant spectral feature, while essentially all the V atoms of the cell would be equivalent, and the effects of the t_{2g} states coming from the few non-equivalent vanadium atoms around the vacancy would be negligible. At present, such a calculation is however computationally unfeasible in the framework of LDA+DMFT.

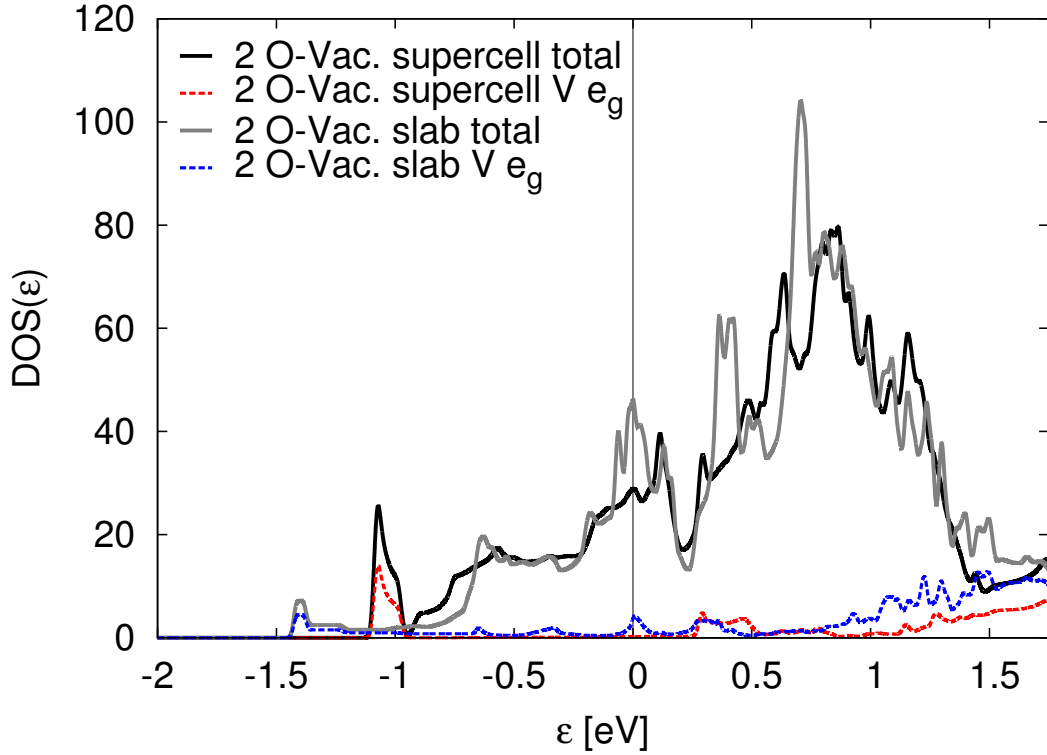**Comparison of DFT results between different oxygen vacancy configurations**

Figure S 7. (Color online) GGA Total and Vanadium e_g resolved density of states (DOS) for $2 \times 2 \times 3$ bulk and the $2 \times 2 \times 4$ slab structures with two oxygen vacancies. See text for details.

In order to strengthen the claim given in the main text regarding the position of the in-gap states, we have also constructed a stoichiometric $2 \times 2 \times 4$ slab of $SrVO_3$ with 20Å of

vacuum and two oxygen vacancies in the VO_2 surface plane. We have relaxed this structure with VASP. Both for the $2 \times 2 \times 3$ bulk and the $2 \times 2 \times 4$ slab structures with two oxygen vacancies we have performed GGA calculations with the full potential local orbital (FPLO) method [SR20] as well as with FPLAPW. We converge the calculations with $12 \times 12 \times 12$ k points in the bulk and $8 \times 8 \times 8$ k points in the slab case. As shown in Fig. S7, we find that the in-gap state for the slab appears around -1.5 eV, and shows a weak dispersion due to the finite size of the slab considered, while the in-gap state for the supercell is at -1 eV. Additionally, we also checked the effects of correlations on that in-gap state via GGA+U calculations, which showed no significant effect on its position. Therefore, we conclude that also LDA+DMFT will not change the position of the in-gap state, as we have already found to be the case in all other calculations we performed. So the LHB will indeed fall in the same position as the in-gap state of Vanadium e_g character when considering an average over various spatial distributions of vacancies.

———————————

* S.B. and T.C.R. contributed equally to this work

† valenti@itp.uni-frankfurt.de

‡ andres.santander@csnsm.in2p3.fr

[SR1] K. Yoshimatsu *et al.*, Dimensional-Crossover-Driven Metal-Insulator Transition in $SrVO_3$ Ultrathin Films, Phys. Rev. Lett. **104**, 147601 (2010).

[SR2] K. Yoshimatsu *et al.*, Metallic Quantum Well States in Artificial Structures of Strongly Correlated Oxides, Science **333**, 319 (2011).

[SR3] M. Kobayashi *et al.*, Origin of the Anomalous Mass Renormalization in Metallic Quantum Well States of Strongly Correlated Oxide $SrVO_3$, Phys. Rev. Lett. **115**, 076801 (2015).

[SR4] M. Takizawa *et al.*, Coherent and incoherent d band dispersions in $SrVO_3$, Phys. Rev. B **80**, 235104 (2009).

[SR5] T. Yoshida *et al.*, Mass renormalization in the bandwidth-controlled Mott-Hubbard systems $SrVO_3$ and $CaVO_3$ studied by angle-resolved photoemission spectroscopy, Phys. Rev. B **82**, 085119 (2010).

[SR6] S. Aizaki *et al.*, Self-Energy on the Low- to High-Energy Electronic Structure of Correlated Metal $SrVO_3$, Phys. Rev. Lett. **109**, 056401 (2012).

[SR7] J. Enkovaara *et al.*, Electronic structure calculations with GPAW: a real space implementation of the projector augmented-wave method, J. Phys.: Condens. Matter **22**, 253202 (2010).

[SR8] S. Backes, D. Guterding, H. O. Jeschke, and R. Valentí, Electronic structure and de Haas - van Alphen frequencies in KFe_2As_2 within LDA+DMFT, New J. Phys. **16**, 083025 (2014).

[SR9] P. Blaha, K. Schwarz, G. K. H. Madsen, D. Kvasnicka, and J. Luitz. An Augmented Plane Wave Plus Local Orbitals Program for Calculating Crystal Properties. vol. **1** (2001).

[SR10] P. Werner, A. Comanac, L. de' Medici, M. Troyer and A. J. Millis, Continuous-Time Solver for Quantum Impurity Models, Phys. Rev. Lett. **97**, 076405 (2006).

[SR11] B. Bauer *et al.*, The ALPS project release 2.0: open source software for strongly correlated systems, J. Stat. Mech. Theory Exp., P05001 (2011).

[SR12] E. Gull, P. Werner, S. Fuchs, B. Surer, T. Pruschke, and M. Troyer, Continuous-time quantum Monte Carlo impurity solvers, Comput. Phys. Commun. **182**, 1078 (2011).

[SR13] M. Aichhorn *et al.*, Dynamical mean-field theory within an augmented plane-wave framework: Assessing electronic correlations in the iron pnictide LaFeAsO, Phys. Rev. B **80**, 085101 (2009).

[SR14] J. Ferber, K. Foyevtsova, H. O. Jeschke and R. Valentí, Unveiling the microscopic nature of correlated organic conductors: The case of κ-$(ET)_2Cu$ $[N(CN)_2]Br_xCl_{1-x}$, Phys. Rev. B **89**, 205106 (2014).

[SR15] A. I. Liechtenstein, V. I. Anisimov, and J. Zaanen. Density functional theory and strong interactions: Orbital ordering in Mott-Hubbard insulators, Phys. Rev. B **52**, R5467 (1995).

[SR16] V. I. Anisimov, I. V. Solovyev, M. A. Korotin, M. T. Czyzyk and G. A. Sawatzky, Density-functional theory and NiO photoemission spectra, Phys. Rev. B **48**, 16929 (1993)

[SR17] S. L. Dudarev, G. A. Botton, S. Y. Savrasov, C. J. Humphreys, and A. P. Sutton, Electron-energy-loss spectra and the structural stability of nickel oxide: An LSDA+U study, Phys. Rev. B **57**, 1505 (1998).

[SR18] K. S. D. Beach, Identifying the maximum entropy method as a special limit of stochastic analytic continuation, arXiv:cond-mat/0403055 (2004) (unpublished).

[SR19] M. Casula *et al.*, Low-Energy Models for Correlated Materials: Bandwidth Renormalization from Coulombic Screening, Phys. Rev. Lett. **109**, 126408 (2012).

[SR20] K. Koepernik and H. Eschrig, Full-potential nonorthogonal local-orbital minimum-basis band-structure scheme, Phys. Rev. B **59**, 1743 (1999); http://www.FPLO.de